Direct measurements of slip in sheared polymer solutions

By L. A. ARCHER[1], R. G. LARSON[2] AND Y.-L. CHEN[3]

[1] Department of Chemical Engineering, Texas A&M University, College Station,
TX 77843-3122, USA

[2] AT&T Bell Laboratories, Murray Hill, NJ 07974, USA

[3] Kelco, 8225 Aero Drive, San Diego, CA 92123-1718, USA

We report direct measurements of slip flow during and after plane-Couette shearing of poly(styrene) solutions between glass surfaces. Slip is studied by visualizing the microscopic motions of micron-sized silica spheres suspended in the solutions. Slip velocities as large as 4 µm s^{-1} are observed during shear, and recoil displacements of as much as 80 µm are observed at the glass surfaces after the driving surface stops moving. Significant slip is observed when the Weissenberg number $\lambda\dot{\gamma}$ exceeds 0.5 or so, where λ is the relaxation time and $\dot{\gamma}$ the shear rate. The magnitude of the slip correlates strongly with the fluid's birefringence, indicating that slip is induced by polymer stress or orientation. Away from the centre of the sample, toward the free edges, a secondary flow is observed, which appears to be driven by a normal-stress imbalance at these edges.

1. Introduction

Significant rheological evidence has emerged, especially in recent years, that shows apparent violations of the no-slip boundary condition in flowing polymer melts and solutions above a certain critical stress σ^* (Benbow & Lamb 1963; Blyler & Hart 1970; Ramamurthy 1986; Kalika & Denn 1987; Lim & Schowalter 1989; Piau, El Kissi & Tremblay 1990; Hatzikiriakos & Dealy, 1991, 1992a, b; Demarquette & Dealy 1992; Chen, Larson & Patel 1994). In melts, this critical stress ranges from 0.1–1.0 MPa, but it can be significantly lower in polymer solutions (Demarquette & Dealy 1992; Chen *et al.* 1994). Slip or stick-slip flow of polymer melts during extrusion has long been thought responsible for 'shark-skin' and 'extrudate distortion' in extruded polymer components. Indeed, some studies have shown that shark-skin distortion can be suppressed by careful choice of the material used to construct the extruder die (Ramamurthy 1986). Other studies have revealed transient pressure drops both during and prior to the formation of shark-skin and extrudate distortion that are suggestive of a stick-slip type flow of the fluid (Lim & Schowalter 1989). Slip flow has also been thought responsible for transient stress decay and stress wave-form distortion in plane-Couette and circular-Couette flow of polymer melts and solutions (Hatzikiriakos & Dealy 1991, 1992a, b; Demarquette & Dealy 1992; Chen *et al.* 1994).

Recently, Archer & Larson (1995) reported apparent violations of the no-slip condition in α-D-glucose, a non-polymeric fluid, at stresses comparable to the critical stress for apparent slip in polymer melts. Moreover, prior to slip, α-D-glucose displays bulk Newtonian rheology; this proves that slip flow is not necessarily limited to bulk non-Newtonian fluids. Other evidence of slip flow in small-molecule fluids has been

obtained in plane-Couette flow of nanometer-thick layers of octamethylcyclo-tetrasiloxane using a 'surface forces' apparatus (Van Alsten & Granick 1988; Reiter, Demirel & Granick 1994). In all these studies, slip flow is inferred from stress measurements, and the degree to which true interfacial slip is responsible for these observations is, therefore, still open to question.

In a recent study, Migler, Hervet & Leger (1993) used an evanescent wave fluorescence technique to measure the slip velocity of a layer of a poly(dimethyl siloxane) (PDMS) melt in contact with a stationary octadecyltrichlorosilane (OTS)-covered quartz plate during shear flow in a plane-Couette flow device. With this technique, the velocity of the melt could be measured in a zone within about 0.1 μm of the solid surface. For a 50 μm thick polymer layer sandwiched between the quartz plates of this device, a transition from 'weak' slip (slip velocities of around 10^{-2} μm s^{-1}), to 'strong' slip (slip velocities as high as 400 μm s^{-1}), was observed at a critical shear rate $\dot{\gamma}_p^* \sim 0.15$ s^{-1}, proving that significant slip can occur in flowing polymer melts at sufficiently high shear rates.

In the present study, we use a simpler method for measuring slip in flowing polymer solutions. In this method, slip is inferred by observing the motion of micron-sized spherical silica particles suspended in the flowing polymer solutions, using an optical microscope. As will be seen, this technique allows slip flow to be visualized easily and makes it possible to measure the fluid velocity as a function of distance from the solid surfaces. Chen & Emrich (1963) used a similar technique involving smoke particles to infer slip in gas flow. For polymers, Galt & Maxwell (1964) used 50 μm particles as tracers in pressure-driven flow of polyethylene melts through circular and rectangular tubes, and used photographs of the particles to infer their velocities. They observed that only a fraction (around $\frac{1}{4}$) of the particles 'at the wall' were motionless; the rest moved with an apparent slip velocity of around 10 % of the centreline velocity. The inference of slip in this study was questioned by den Otter *et al.* (1967), who observed that the large size of the particles and the photographic technique used by Galt & Maxwell cast doubt on the assumption that velocities 'at the wall' were being probed. In the studies of den Otter, Wales & Schijf, who used 5–20 μm dust particles as probes, no evidence of slip was found in melts of polyethylene and poly(dimethylsiloxane).

In the work presented here, much smaller particles are used (1.5 μm), so that velocities closer to the wall can be probed. In addition, we measure time-dependent slip after the driving force for bulk flow is removed, and find that the highest velocities are at the wall, which is a result that could not be an artifact of bulk flow. In the following sections we present a detailed study of slip flow in poly(styrene) solutions in simple shear flow.

2. Experiment

2.1. *Samples*

Solutions containing 8 and 20 weight % poly(styrene) with molecular weight $\overline{M}_w = 2 \times 10^6$ and polydispersity index $\overline{M}_w/\overline{M}_n = 1.3$ (PS-8 and PS-20, respectively) in tricrecyl phosphate (TCP) are prepared by dissolving the respective poly(styrene)–TCP mixtures in an excess of toluene. To prepare samples for optical microscopy experiments, a few tenths of a percent of 1.5 μm diameter spherical silica particles are added to some PS-8 and PS20 solutions. In these samples, a uniform distribution of silica particles is achieved by gently stirring the mixture as toluene slowly evaporates at room temperature. Both batches of polymer solution, with and without silica particles, are subsequently heated under vacuum for 6–7 days at around 55 °C to

remove any remaining traces of toluene. The particle-free poly(styrene)–TCP solutions are used for birefringence and shear stress measurements.

2.2. *Method*

2.2.1. *Microscopy*

To investigate slip flow in polymer solutions, poly(styrene) solutions containing silica spheres are sandwiched between glass plates in a plane-Couette flow device attached to the sample stage of an optical microscope. This microscope is equipped with a video camera interfaced with a video recorder with time-lapse capabilities, which allows convenient transient measurement of slow or rapid motions of the particles in the microscope's field of view. The plane-Couette flow device used in this study is depicted in figure 1, and consists of two borosilicate glass plates of length $L = 10$ cm and width $W = 2.5$ cm attached to a motorized translation stage and a stationary aluminium block, respectively. In this device, the sample is bounded around the edge only by the meniscus it forms against air. Shear flow is generated by motion of the top plate using a stepper motor; the shear rate and shear strain are set by the velocity and travel time, respectively, of the moving plate. Moreover, by adjusting the vertical displacement of the upper glass plate with a micrometer-driven translation stage to which it is attached, the thickness of the polymer solution layer sandwiched between them can be varied, thus permitting the gap dependence of the velocity profile to be investigated. Parallelism of the two plates is achieved by bringing them into contact, and then adjusting the orientation of the lower plate using micrometers attached to ball-bearing mounts, as discussed elsewhere (Larson & Mead 1992).

In all experiments, the flow cell is mounted on a stage that allows 'x, y, z' positioning with respect to the microscope objective. This makes investigation of spatial variations in the flow field possible. For example, by adjusting the vertical distance between the flow cell and the microscope objective, the motion of particles at various distances from the shearing surfaces can be monitored. Similarly, by moving the flow cell in the 'neutral' direction, the flow profile at various distances from the edge of the cell can be studied. All measurements are made at room temperature, around 23 ± 1 °C. The apparent depth of the particle in the sample must be corrected by accounting for the index of refraction, which we measure to be around 1.2 for our solutions.

2.2.2. *Birefringence*

The optical train used in our birefringence experiments is presented in figure 2. This arrangement is considered in great detail elsewhere (Johnson, Fratini & Fuller 1985; Fuller 1990), and it can be shown that the signal measured by the photodiode is of the form

$$I = I_0(1 + 2 \sin \delta' J_1(A) \sin(\omega t)), \tag{1}$$

where I_0 is the light intensity incident on the sample, ω is the polarization modulation frequency, $J_1(A)$ is a Bessel function coefficient that results from the modulation, and $\delta' = 2\pi d \Delta n'/\lambda$ is the birefringence retardation. Here d is the sample thickness, λ the wavelength of the incident light, and $\Delta n' = n'_{xx} - n'_{zz}$ is the sample's birefringence. It is therefore apparent that provided $J_1(A)$ is known, the flow birefringence of our poly(styrene) solutions may be recorded from the ratio of the Fourier coefficients of the optical signal. In the present study, the relevant Fourier coefficients are recovered using a low-pass filter, which measures the static portion of the signal, and a lock-in amplifier tuned to the modulation frequency ω, which measures the time-dependent part of the optical signal.
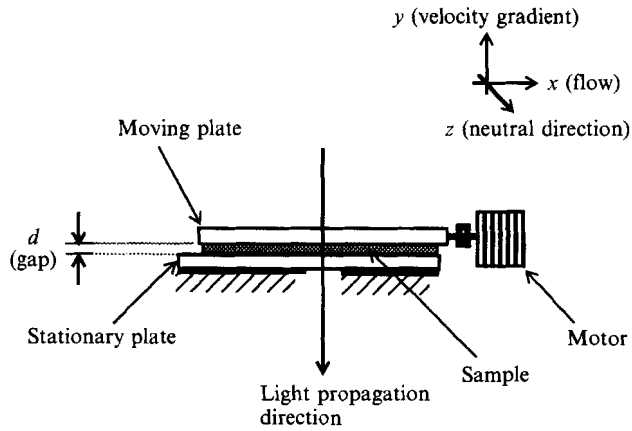
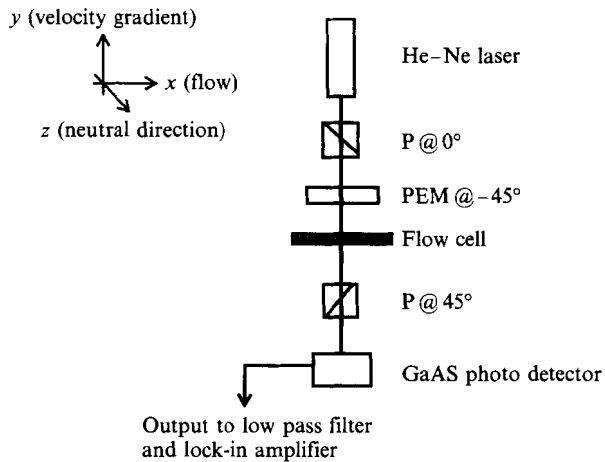FIGURE 1. Diagram of plane-Couette cell, showing the flow geometry.

FIGURE 2. Optical train for birefringence experiments.

Samples of particle-free PS-20 sandwiched between the glass plates of the plane-Couette flow cell described in the last section are used for birefringence measurements. As before, measurements are all carried out at room temperature.

2.2.3. *Shear stress*

The complex moduli of PS-8 and PS-20 in oscillatory shear, and the time-dependent shear stress of PS-20 in steady shear are studied using a Rheometrics System IV rheometer. All measurements are conducted at room temperature using 50 mm diameter stainless steel cone-and-plate fixtures.

3. Results

3.1. *Shear stress*

Dynamic storage (G') and loss (G'') moduli of PS-20 and PS-8 are presented in figures 3(a) and 3(b), respectively. The open symbols are for samples containing silica particles, and the filled symbols are for the particle-free samples. A strain amplitude of
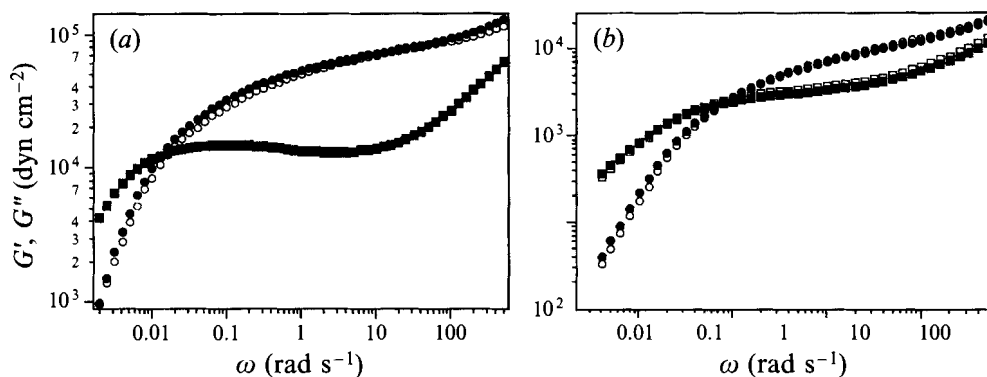
FIGURE 3. Storage G' (●, ○) and loss G'' (■, □) moduli of (a) 20% and (b) 8% poly(styrene) solutions in tricrecyl phosphate with and without silica particles (filled and open symbols respectively). All data were collected at room temperature using a strain amplitude of 30%.
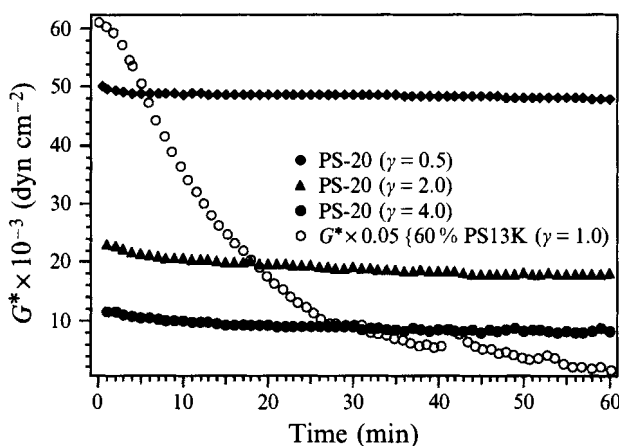
FIGURE 4. Time-dependent complex moduli of 20% poly(styrene) solutions at a shear frequency of 0.5 rad s⁻¹, and for shear strains varying from 1.0 to 5.0, along with similar results for 60% PS13K at a strain of unity.

30% is used in all experiments. This amplitude is chosen to obtain sufficiently high torques to permit accurate characterization of the low-frequency terminal behaviour of these solutions. These plots show that the dynamical mechanical properties as well as the approximate relaxation time λ (inverse of the frequency at which the storage and loss moduli intersect) of each material is largely unaffected by the presence of the micron-sized silica particles in the material. The silica particles, therefore, do not disrupt the flow of these fluids and thus function only as flow tracers. The relaxation time λ of PS-20 is 66 s and for PS-8 it is 1.2 s. Furthermore, the low-frequency viscosity η_0 of PS-8 is 10^4 P and the density ρ_s of TCP is 1.2 g cm⁻³, of silica ρ_p is 2.2 g cm⁻³, and of poly(styrene) is 1.08 g cm⁻³. Thus the settling velocity $V \approx a^2 (\rho_p - \rho_s) g/(18\eta_0)$ of the $a = 1.5\,\mu$m diameter silica particles used in this work is no greater than 2×10^{-10} cm s⁻¹ in either PS-20 or PS-8. As a result, particle settling is expected to be negligible in flowing PS-8 and PS-20 under the conditions of our experiments.

The complex modulus ($G^* = (G'^2 + G''^2)^{1/2}$) of PS-20 is only about 10^5 dyn cm⁻² at the highest frequencies. This value is some five times lower than the critical stress at
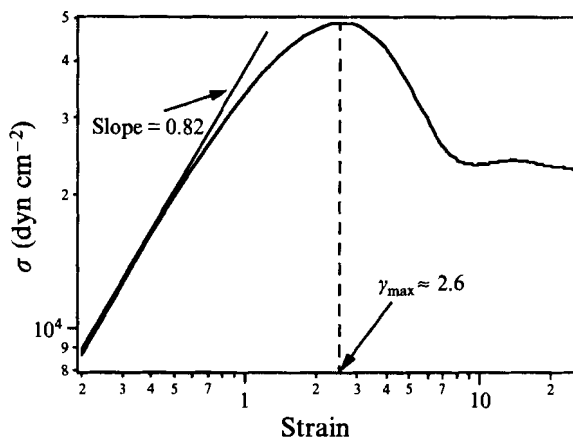
FIGURE 5. Shear stress *vs.* shear strain for PS-20 at a shear rate of 0.5 s^{-1}. This plot shows that a stress overshoot occurs for this material at a strain of about 2.6.

which gross stress decay, thought to be caused by slip, is observed in more concentrated polymer solutions and melts (Chen *et al.* 1994). In figure 4, G^* is observed to decrease only by about 30% after an hour of prolonged oscillatory shearing of PS-30 at strain amplitudes as high as 4.0, while it decreases by more than an order of magnitude in a similar time period when a 60% poly(styrene) ($M_w = 13000$) solution in TCP is continuously sheared at a strain amplitude of 1.0 (Chen *et al.* 1994). From these measurements it appears that the apparent 'slip' flow responsible for massive stress decay in the 60% poly(styrene) solution, does not occur in PS-20 under the conditions studied here. The 30% decrease in G^* observed in PS-20 accumulates slowly during an hour of continuous shearing, and is thus reminiscent of shear-induced diffusion effects described elsewhere (Larson 1992b; Madga *et al.* 1993). The duration of the direct slip measurements reported in the following sections are at most a couple of minutes. Thus the slow decrease in G^*, whatever its origin, is unlikely to play a significant role in what follows.

The strain dependence of the shear stress of PS-20 after start-up of steady shearing at a shear rate of 0.5 s^{-1} is presented in figure 5. Here the shear stress is observed to increase with strain γ as $\gamma^{0.82}$ at small strains and displays an overshoot at a strain of about 2.6.

3.2. *Birefringence*

In figure 6 the transient birefringence following the cessation of flow is observed to decay at similar rates for strains ranging from 0.5 to 4.0. The longest time constant for this decay ranges from 65 to 68 s, which is roughly equal to the molecular relaxation time λ recovered from the dynamic moduli G' and G''. At low strains, after start-up of steady shearing, the birefringence scales like $\gamma^{1.6}$, which is stronger than the strain dependence of the shear stress; compare figures 5 and 7. Furthermore, at a strain of 4.4, the birefringence displays an overshoot, and subsequently decreases with strain at higher strains, see figure 7(*a*). Figure 7(*b*) shows that the shear-rate dependence of the birefringence is slightly weaker than linear at the lowest rates measured. At very low shear rates, $\lambda\dot{\gamma} \ll 1$, $\Delta n'$ is expected to increase quadratically with increasing shear rate, but this regime is not explored here.
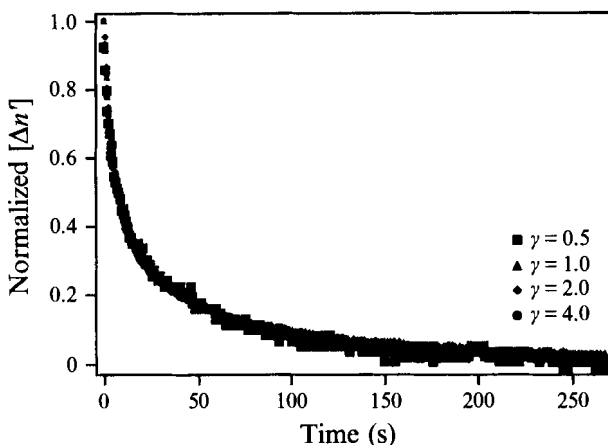
FIGURE 6. Transient birefringence at various strains for PS-20. The birefringence plots are normalized by the value of the birefringence immediately after flow ceases.
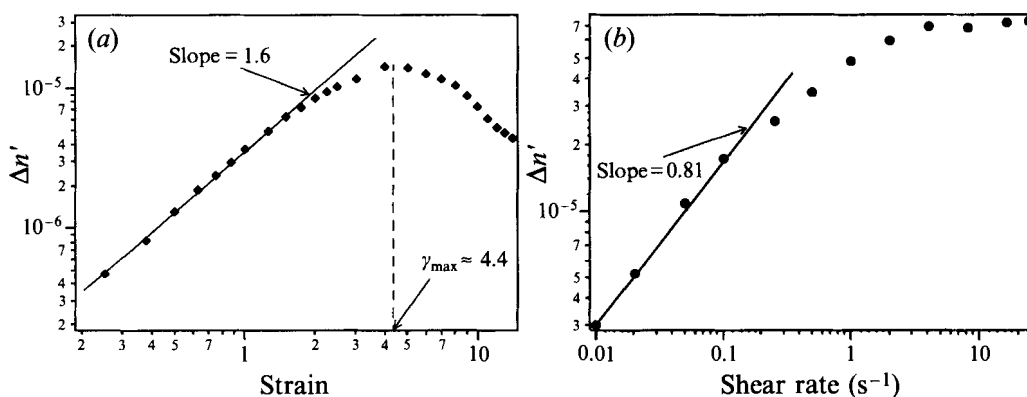

FIGURE 7. (*a*) Birefringence *vs.* strain for a shear rate of 0.5 s^{-1} for PS-20. The birefringence increases with strain as $\gamma^{1.6}$ at low strains and goes through an overshoot at a strain of about 4.4. (*b*) Birefringence *vs.* shear rate at a strain of 5.0 for PS-20.

3.3. *Microscopy*

Microscopy measurements reveal that particles in contact or very nearly in contact with the lower stationary plate of the plane-Couette flow cell move during flow. If no slippage occurs between the polymer solution and the glass at the lower plate, these particles would be expected to remain stationary at all times. However, from figure 8 (*a*) it is evident that although the particles are motionless (zero slip displacement) during the first several seconds of flow (insert), they gradually begin to move at later times. The strain at which the transition from stick to slip is observed appears to be around 0.5, and is roughly independent of the shear rate. The transition from stick to slip revealed by observing the motion of a particle is not caused by a displacement of that particle away from the solid surface, because the same particle undergoes this transition repeatedly, if the stress is allowed to relax between runs. For a Newtonian poly(dimethyl siloxane) melt, no motion of suspended particles was observed at the stationary plate either during or after shear flow.

When the data of figure 8 (*a*) are replotted on a linear scale, as in figure 8 (*b*), they show an approach to a constant slope at large strains, implying that the *slip velocity*
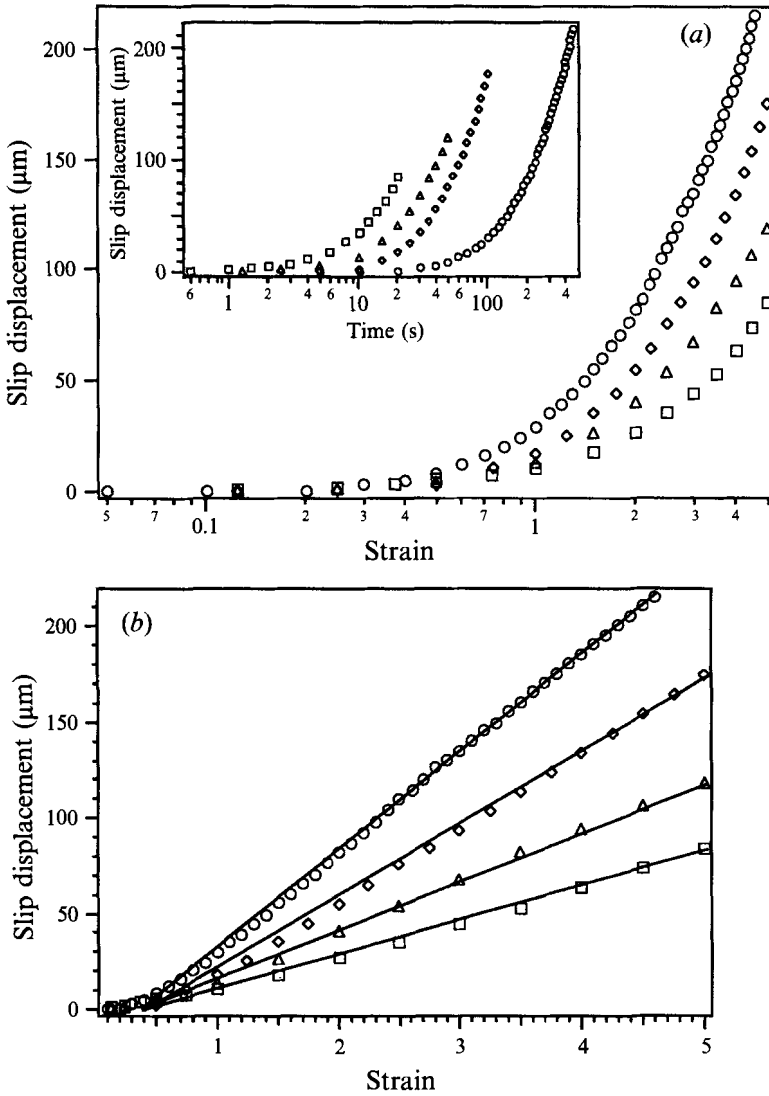
FIGURE 8. (a) Slip displacement at lower plate during flow vs. strain and time (insert) at various shear rates: $\square$, $\dot{\gamma} = 0.25$ s^{-1}; $\triangle$, $\dot{\gamma} = 0.1$ s^{-1}; $\diamondsuit$, $\dot{\gamma} = 0.05$ s^{-1}; $\bigcirc$, $\dot{\gamma} = 0.01$ s^{-1}. This plot shows that there is little, if any, slip in the early stages of flow (low strains), but slip increases dramatically at strains in excess of about 0.5 for a cell gap of 500 μm. (b) The same as (a), on a linear scale.

V_s becomes nearly constant in time. We find that the high-strain value of V_s increases roughly as $\dot{\gamma}^{2/3}$ from $V_s = 0.53$ μm s^{-1} to 4.4 μm s^{-1} as the shear rate $\dot{\gamma}$ increases from 0.01 to 0.25. This implies that the so-called *extrapolation length* $b \equiv V_s/\dot{\gamma}$ is a weakly decreasing function of shear rate with an average value of around 40 μm for PS-20 over shear rates in this range. Note that the extrapolation length is *not* the slip displacement plotted in figure 8; instead b is the apparent distance below the liquid–solid interface at which a linear velocity profile with slip velocity V_s extrapolates to zero velocity. For small-molecule liquids, such as water flow through capillaries with hydrophobic surfaces, the extrapolation length is typically of the order of several times the molecular diameter (Churaev, Sobolev & Somov 1984; Blake 1990). By this standard, an extrapolation length of 40 μm is very large.
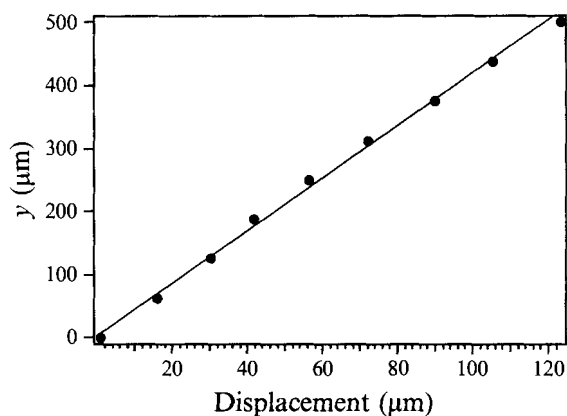
FIGURE 9. Particle displacement at various distances, y, from the lower plate of the plane-Couette flow cells as a result of shearing at a rate of 0.5 s^{-1} and a shear strain of 0.25, for a gap of 500 μm. Distances in the flow cell are measured using a stage driven by a screw micrometer, which adjusts the distance between the flow cell and the microscope objective. The profile is linear, as expected for a simple shear flow.
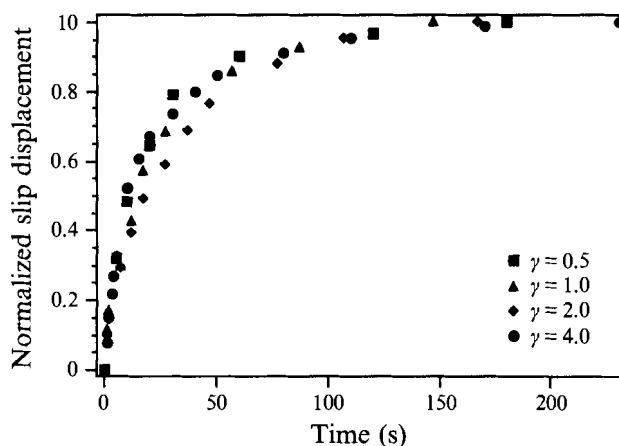

FIGURE 10. Slip displacement, normalized to unity at long times, *vs.* time at the upper surface following cessation of shear flow, for strains ranging from 0.5 to 4.0, and a gap of 500 μm.

The displacement of particles during flow at a small strain of 0.25, lower than the critical strain for slip, is presented in figure 9, and is clearly a linear function of location, y, in the gap. This linear profile is the expected one for simple shear flow and the displacements at the upper and lower plates are precisely those expected for a 25% strain, demonstrating that slip flow is absent at this low strain. Such a profile is also useful since it allows us to determine the location of particles in the gap to within a few microns by simply monitoring their displacements at low strains. This method was used to establish the y-coordinate of the particles more accurately than is possible using the focal positions of the particles as viewed through the microscope. The y-coordinates determined this way were used for the abscissas in figure 12(a–c).

The particles are also observed to travel large distances following the cessation of flow. Such motion is clearly not expected if the solution at the upper glass surface remains attached to this surface; this motion therefore also results from slippage
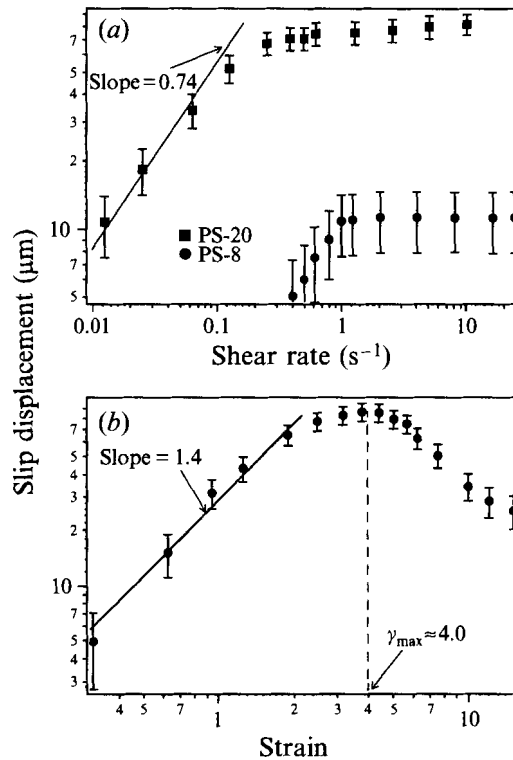
FIGURE 11. (*a*) Slip displacement at the upper plate following flow of PS-20 and PS-8 at various shear rates, for a strain $\gamma = 5.0$. (*b*) Slip displacement at the upper plate following flow of PS-20 at various strains. At low strains, the displacement increases with strain as $\gamma^{1.4}$, and displays an overshoot at a strain of about 4.0. These experiments are conducted using a gap of 500 µm.

between the polymer solution and the upper surface, and its magnitude directly measures the slip displacement of the fluid. Particles in contact with the upper surface manifest such motion by travelling distances as high as 80 µm in a direction opposite to the initial flow direction after the flow is stopped. The transient decay of the slip velocity after cessation of bulk shear is similar for all imposed strains (figure 10). The longest time constant of this decay is around 58 s, which is close to the relaxation time of the polymer chains in PS-20 (around 66 s). Also, the initial slope of the slip displacement versus time yields an initial slip velocity after cessation of shearing which is in good agreement with the slip velocity at large strains after start-up of shearing. Thus, when shear stops, the slip velocity on the upper surface does not instantaneously change, but instead decays with a time constant similar to that governing viscoelastic stress relaxation.

From figure 11(*a*) it is apparent that, at low shear rates, the magnitude of the slip displacement following the cessation of shearing scales with the shear rate $\dot{\gamma}$ as $\dot{\gamma}^{0.74}$, and reaches a plateau at higher rates. It is also apparent that the amount of slip achievable in PS-20 is significantly greater than that observed in PS-8, and that measurable slip is observed at much lower shear rates in PS-20 than PS-8. The error bars in this and all other plots presented in the article are estimated from the run-to-run variability of the measurements. From figure 11 (*a*), we find that slip displacements greater than 5 µm occur in PS-8 when $\dot{\gamma} > 0.4$ s^{-1}, and for PS-20, slip displacements of this magnitude are estimated to occur for $\dot{\gamma} \approx 0.004$ s^{-1}. These values of the shear rate

correspond to Weissenberg numbers, $\lambda\dot{\gamma}$, of 0.5 and 0.25, respectively, for PS-8 and PS-20.

The strain dependence of the slip displacement at the upper plate is presented in figure 11(*b*). At low strains, the slip displacement scales with strain γ as $\gamma^{1.4}$, and displays an overshoot at a strain of around 4.0. At higher strains, the slip displacement gradually decreases with increasing strain. These measurements are all made at a shear rate of 0.5 s^{-1}. These features of the strain dependence of the slip displacement are very similar to those for the birefringence; compare figures 7(*a*) and 11(*a*). The closer correspondence of slip displacement with the birefringence than with the shear stress (figure 5) indicates that the slip flow following simple shear is driven by the orientation of polymer strands (normal stresses) in the flow plane rather than by the shear stress. Like the birefringence, the slip displacement is also nearly a linear function of shear rate at low rates (figure 7*b*) and displays a much weaker shear-rate dependence at higher rates. The decay time constant of the slip displacement following cessation of shearing is also close to that of the birefringence; compare figures 6 and 10.

Unlike the fluid at the upper surface, which slips in a direction opposite to the direction of the imposed shear following flow, fluid elements in contact with the lower stationary plate are found to continue moving in the direction of flow after the motion of the upper surface has stopped. In fact, at the lower stationary surface, there is no sudden change in the particle velocity when the upper surface stops moving. Instead, the particles initially continue moving in the same direction as they did during the shearing flow, and then gradually slow to a halt with a time constant roughly equal to the fluid's relaxation time, which is consistent with the behaviour of the slip velocity at the upper surface. At various intermediate locations in the cell, motion varies uniformly from recoil (close to the top surface) to continued movement in the direction of flow (close to the bottom surface). Near the centre of the cell, $y = \frac{1}{2}d$, no motion of the particles is observed, and the flow profile *vs.* gap is S-shaped, with the slip displacement being roughly of equal magnitude at the top and bottom plates (figure 12(*a*)). This peculiar shape of the displacement profile might be influenced by a secondary flow, discussed shortly. A constant strain of 5.0 and a shear rate of 0.5 s^{-1} was used in these measurements. In this plot motion opposite to the flow direction is designated negative.

Using the x, y, z stage to adjust the position of the flow cell relative to the focal position of the microscope, we can examine the displacement profiles at various locations in the (x, z)-plane. Figures 12(*b*) and 12(*c*) show the displacement profiles at locations $x = \mp 1.25$ cm upstream and downstream, respectively, of the centre of the cell ($x = 0, z = 0$) at a gap of 500 μm. Note that the profiles in these off-centre locations are asymmetric, such that for $x < 0$ (figure 12*b*) there is a net flow in the positive direction, while for $x > 0$ (figure 12*c*) there is a net flow in the negative direction. Thus in both cases the net flow is towards the centre of the cell. The magnitude of the velocity v_x at the midpoint in the gap ($y = \frac{1}{2}d$) immediately after flow stops is around 1.5 μm s^{-1} at $x = \mp 1.25$. At $x = 0$, this midpoint velocity is zero and there is not net upstream or downstream flow; see figure 12(*a*).

Since the x-component of the velocity, v_x, varies with x, conservation of mass implies that the z-component of the velocity, v_z, must vary with z, assuming that there is no flow in the y-direction perpendicular to the plates. As noted above, $v_z = 0$ along the x-axis at $z = 0$. Hence for $z \neq 0$, v_z must be non-zero. And, indeed, when the sample is examined along the axis $x = 0$ at z-locations away from the central location at $z = 0$, we observe bulk flow towards the edges of the sample after cessation of shear. Figure 13 shows the particle displacement D_z in the neutral direction (z) at various positions
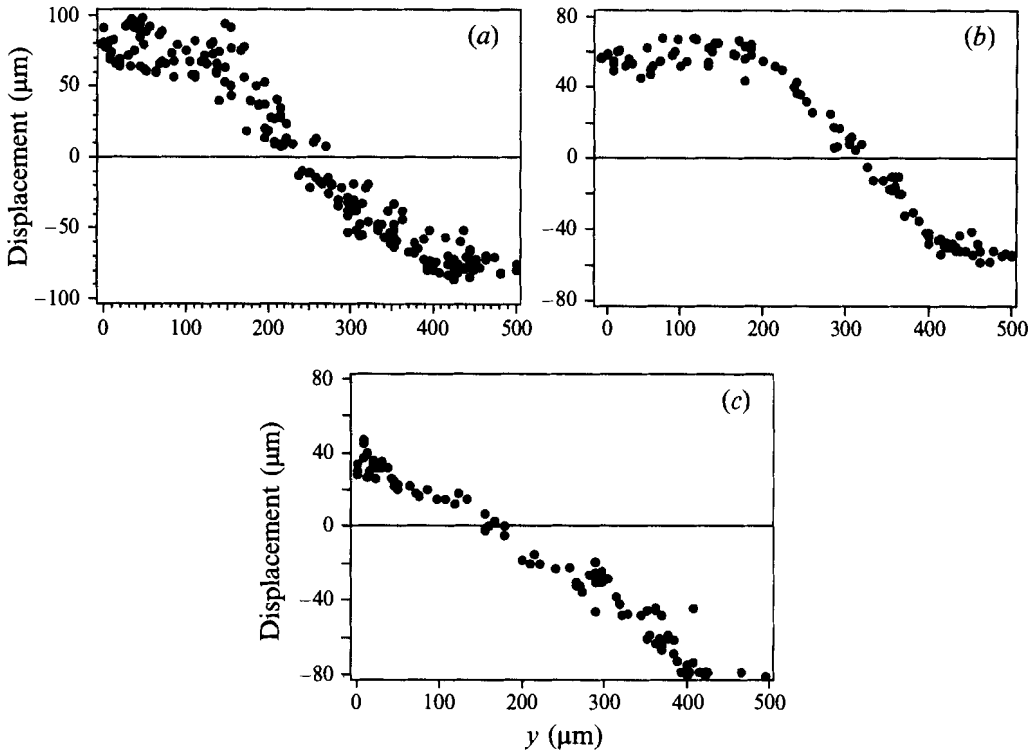
FIGURE 12. Particle displacement following flow at various distances, y, from the lower plate of the flow cell, for a 500 µm gap. Profiles are obtained (a) close to the centre of the (x, z)-plane of the sample, (b) 1.25 cm upstream of the central location investigated in (a), (c) 1.24 cm downstream of the central location.
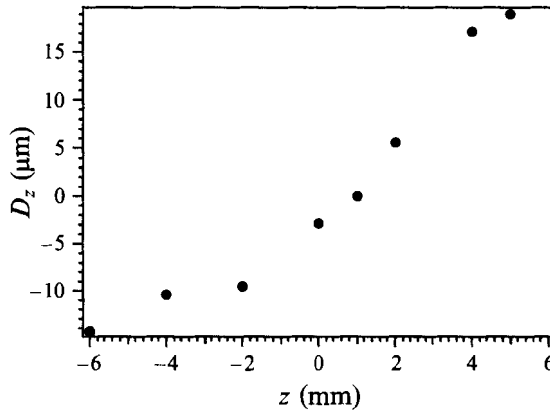

FIGURE 13. Particle displacement in the neutral direction (D_z) at various distances (along the neutral direction, z) from the centre, measured at a location slightly above the midpoint in the gap, for a gap of 500 µm. Locations to the left of centre, along the neutral direction z, and the component of the fluid displacement in this direction, are arbitrarily designated negative.

z, for a y-value around 30 µm above the mid-plane of the sample $(y = \frac{1}{2}d)$. This plot shows that D_z is positive for $z > 0$, and negative for $z < 0$, indicating that there is side-to-side flow of the fluid away from the centre of the cell.

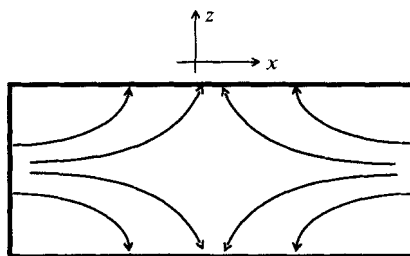These results, together with the variations in v_x along the x-direction, show that the

FIGURE 14. Sketch of the aerial flow pattern in the (x, z)-plane of the fluid close to the midplane of a cell of dimensions 4×1 in.
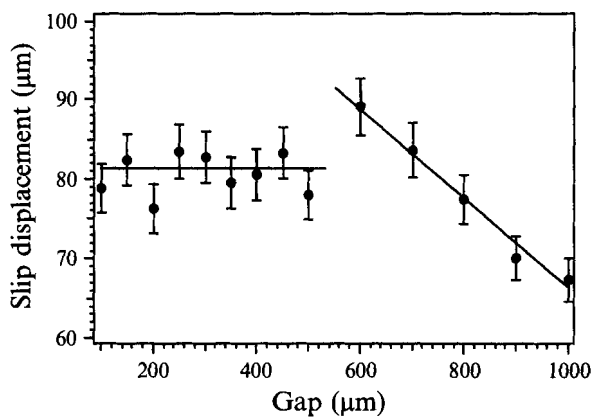

FIGURE 15. Plot of slip displacement *vs.* gap d ranging from 100 to 1000 μm. Slip is measured by monitoring the motion of particles at the upper plate. At low gaps, the slip displacement is independent of gap, but for gaps in excess of about 550 μm the slip displacement decreases somewhat with increasing gap.

flow in the bulk of the sample has a general form similar to that depicted in figure 14. The existence of such a flow is reinforced by our observation that after repeated shearing, a sample bulges out to the sides of the cell to a greater extent than just after loading. A dramatic manifestation of this 'bulging' phenomenon has recently been reported in plane-Couette shear flow of molten polyethylene (Koran 1994).

This flow is similar to that of Hele-Shaw flow between flat plates with a pressure drop imposed between the ends of the sample at $x = \pm\frac{1}{2}L$ and the sides at $z = \pm\frac{1}{2}W$. A possible mechanism that might produce such a flow is discussed below. We note here, however, that away from the centre of the sample the aerial flow pattern can vary somewhat from one sample loading to the next, and seems to be sensitive to the location and shape of the menisci bounding the sample on all asides. At the centre of the sample in the (x, y)-plane, however, the profile is insensitive to these details.

In figure 15 the slip displacement is observed to be independent of the cell gap (d) for gaps lower than around 550 μm, but decreases gradually with increasing gap at higher gaps. It appears that a flow transition occurs somewhere between a cell gap of 500 and 600 μm. In fact if a flow profile similar to figure 12(a) is measured using a 0.9 mm gap (figure 16), much more curvature is apparent than in the profile at the lower gap; for example, while the profile close to either plate at a gap of 500 μm is essentially flat, the profile for a gap of 0.9 mm displays a distinct maximum close to the upper plate and a somewhat weaker minimum close to the bottom plate. Thus, the secondary
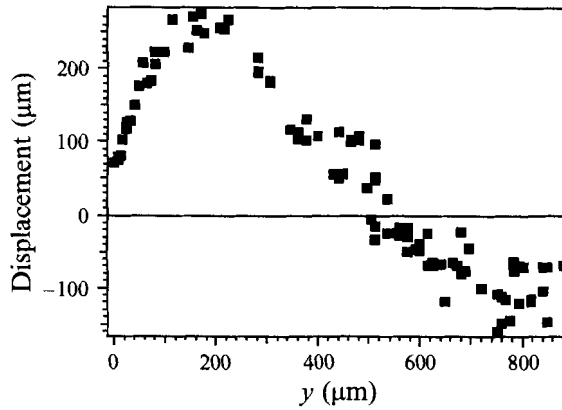
FIGURE 16. Displacement following flow at various distances, y, from the lower plate of the flow cell for a 0.9 mm gap. As in figure 12(a), these measurements are made close to the centre of the cell in the (x, z)-plane.

'Hele-Shaw' flow seems to extend throughout the sample at this large gap, which is not surprising since this type of flow is expected to become more pronounced as the gap increases; see §4.

4. Discussion

The results presented here demonstrate the existence of slip flow in polymeric solutions above a critical stress level. The small, 1.5 μm, size of the particles and their proximity to the surfaces of the shear cell imply that the slip flow occurs within a micron or so of the surfaces, which is consistent with the results of the evanescent wave fluorescence measurements of Migler *et al.* In addition, our technique can measure even small levels of slip, down to a few microns or so. Thus we have no difficulty quantifying slip even for polymers against untreated glass surfaces, to which they appear to adhere rather strongly.

Artifacts that might produce only the illusion of a slip phenomenon are of negligible importance. For example, the distance that a particle will be rolled or convected along a solid surface in the absence of slip is $\sim \frac{1}{2}a\gamma$ where a is the particle diameter and γ is the strain. In our experiments $\gamma \leqslant 5$ and $a \approx 1.5$ μm, so this artifact will contribute only 3.75 μm to the apparent slip, compared to measured slip displacements of 80 μm or more. Furthermore, most of the data presented here were obtained after cessation of the externally driven flow, and under these conditions the maximum particle motions were those of particles nearest to the solid surfaces, an observation that can only be attributed to the existence of slip planes near these surfaces. The large motions of the particles at the glass surfaces are also not caused by migration of particles away from the surfaces into the bulk flowing solution, because the stick-to-slip transition in figure 8 can be observed repeatedly for a given particle, and the settling velocity is too small for significant vertical drift of the particles to occur during our experiments. Prieve, Jhon & Koenig (1985) have observed particle migration across streamlines during shearing of viscoelastic fluids, but only during continuous shearing, and for particles hundreds of times larger than those used here. The speed of the viscoelastic wave that propagates from the upper to the lower surface when the upper surface begins to move is roughly $(G/\rho)^{1/2}$, where G is the fluid's elastic modulus and ρ its density. This wave speed is estimated to be around 100 cm s^{-1} or higher for both

PS-8 and PS-20; hence the wave will reach the bottom stationary surface within a negligible time period of about 10^{-3} s or so after the top surface begins moving. Of course, we cannot rule out the possibility that the slip occurs not exactly at the glass surface but somewhere within a micron-thick layer of fluid adhering to that surface. But it is appropriate to conclude from our data that slip occurs within an order of magnitude of the molecular lengthscale, since the radius of gyration of the polymer molecules is typically around 0.03 μm.

Our studies indicate that slip is induced by polymer orientation, or equivalently, polymer stress. This conclusion is derived from the observation that slip begins to occur only after imposition of a strain of around 0.5. In addition, the slip continues even after bulk flow, driven by motion of the upper plate, ceases. This 'recoil' slip dies out with a time constant equal to the viscoelastic relaxation time of the stress or birefringence. Furthermore, the dependence of the slip displacement on the shear rate or strain mirrors that of the birefringence, again implying that stress or polymer orientation induces slip.

For PS-20, the magnitude of the slip displacement on each of the two solid surfaces is as high as 80 μm for an imposed strain of 5, and is insensitive to gap for gaps of 500 μm or less. For a gap of 500 μm, this yields a slip strain of $(80+80)/500 = 0.32$, which is around 6.4% of the imposed strain of 5. Thus, for gaps of 500 μm or greater, corrections to rheological data required to account for slip should be small or negligible. For smaller gaps, however, this correction can be significant. For example, for a gap of 50 μm, 64% of the imposed strain is lost as a result of slip! Gap-dependent corrections to the shear strain or shear rate of this order of magnitude have also been reported by Hatzikiriakos & Dealy for a poly(ethylene) melt in a sliding plate rheometer (Hatzikiriakos & Dealy, 1991). In those studies, the level of slip was inferred from the dependence of stress on apparent shear rate at various gaps, under the assumption that the slip velocity is independent of gap (an assumption that is supported by our experiments, at least for gaps less than 500 μm).

From the data of Hatzikiriakos & Dealy, an extrapolation length $b = V_s/\dot{\gamma}$ (V_s being the slip velocity) of around 40 μm can be inferred for a poly(ethylene) melt both in plane-Couette and Poiseuille flow, which is similar to the extrapolation length we find for PS-20. This lengthscale is much greater than the size of the macromolecules, and raises questions about its origin. Brochard & de Gennes (1992) have developed a theory for slip of entangled polymeric fluids in which they assume that some polymer chains are tethered to the solid surface by adsorption. At a critical shear stress, these chains undergo a coil–stretch transition and disentangle from the chains in the bulk, creating a slip layer near the surface with a frictional resistance equal to that of an unentangled polymer fluid. In this theory the extrapolation length b_∞ at high stresses is equal to b_0, a molecular slip length, times a large factor proportional to the ratio of the viscosity of the entangled polymeric liquid to that of an unentangled 'monomeric' fluid. For PS-8 and PS-20, the measured extrapolation lengths are around 4 and 40 μm, respectively, which are respectively 100 and 1000 times larger than the radii of gyration of the polymer molecules. These large extrapolation lengths are compatible with values of b_∞ predicted by the theory of Brochard & de Gennes, but follow a scaling closer to $b_\infty \sim \eta^{1/2}$ than to the theoretical scaling $b_\infty \sim \eta$, since the viscosity of PS-20 is 100 times that of PS-8, but the extrapolation lengths only differ by a factor of 10. However, no firm conclusion about the validity of the theory can be made because the density of chains adhering to the surface enters the equations of Brochard & de Gennes, and this quantity may not be the same for PS-8 and PS-20.

If the extrapolation length continues to increase, even only as $\eta^{1/2}$, with increased

polymer concentration or molecular weight, then for highly entangled poly(styrene) solutions with viscosities of the order of 10^9 or so, the extrapolation length might approach the gap used in typical rheological measurements. In that case, slip flow would grossly affect the measured rheological data. Indeed Archer, Chen & Larson (1995) have recently shown that massive levels of slip in highly entangled poly(styrene)-TCP solutions can help explain anomalous rheological data previously reported for these fluids by Larson, Khan & Raju (1988).

Finally, we suggest a mechanism for the in-plane Hele–Shaw-like flow observed away from the centre of the sample (figure 14). As pointed out earlier, such a flow can be produced by a *normal-stress imbalance* at the free edges of the sample. In a viscoelastic fluid, the imposition of a shear strain in the plane-Couette flow geometry produces normal stresses $\sigma_{xx} - p$, $\sigma_{yy} - p$, and $\sigma_{zz} - p$ within the fluid. Here the σ are the viscoelastic normal stresses, and p is an isotropic pressure-like contribution to the stress tensor. At the unbounded edges of the sample, however, the normal stresses are set by the atmospheric pressure, p_{atm}, plus a contribution from surface tension, which we will neglect for simplicity. Thus, along the menisci bounding the fluid at $x = \pm \frac{1}{2}L$, the effective boundary condition is $\sigma_{xx} - p = -p_{atm}$, while the boundary condition along the menisci at $z = \pm \frac{1}{2}W$ is $\sigma_{zz} - p = -p_{atm}$. But in the bulk of the fluid $\sigma_{xx} - \sigma_{zz} \equiv N_3$, the third normal stress difference induced by the flow, is non-zero and, provided the stress-optical rule holds, is proportional to the so-called 1–3 birefringence $\Delta n' = n'_{11} - n'_{33}$ (Ferry 1980), which we measure in our birefringence experiments. The condition, $\sigma_{xx} - \sigma_{zz} = N_3 \neq 0$, is only compatible with the boundary conditions $\sigma_{xx} - p = -p_{atm}$ at one boundary and $\sigma_{zz} - p = -p_{atm}$ at another boundary if p depends on the coordinates x and z. Thus, *there must be a bulk secondary flow that generates a pressure gradient sufficient to offset the incompatibility in the boundary conditions.*

A realistic analysis of this secondary flow would require solving a time-dependent multi-dimensional viscoelastic flow with complex boundary conditions to reflect the shape and movement of the fluid–air menisci. We shall limit ourselves here to a crude analysis from which we estimate the order of magnitude of the secondary flow velocity. We assume that it has the form $V_x = v_x(x, z)$, $V_z = v_z(x, z)$, and $V_y = 0$. Furthermore, immediately after the upper surface comes to a halt, the stress experienced by the fluid is the stress produced by the imposed shear strain. If inertial terms are neglected and gradients of the velocity in the flow-gradient (y) direction are assumed to be much larger than those in the x- and z-directions (the narrow-gap approximation), the quasi-steady-state equations of motion for a constant-viscosity fluid (such as a Maxwell fluid), then become

$$\eta \frac{\partial^2 v_x}{\partial y^2} = \frac{\partial p}{\partial x}, \tag{2}$$

$$\eta \frac{\partial^2 v_z}{\partial y^2} = \frac{\partial p}{\partial z}. \tag{3}$$

Since slip occurs at the surfaces, the appropriate stress-dependent, or shear-rate-dependent, boundary conditions to apply to (2) and (3) are not obvious. For simplicity, we assume that slip is present in the x-direction only, and take

$$v_x = V_s, \quad y = 0,$$
$$v_x = -V_s, \quad y = d,$$
$$v_z = 0, \quad y = 0, d.$$

Subject to these conditions, the solution of (2) and (3) is

$$v_x = V_s\left(1 - \frac{2y}{d}\right) + \frac{1}{2\eta}\frac{\partial p}{\partial x}y(y-d), \tag{4}$$

$$v_z = \frac{1}{2\eta}\frac{\partial p}{\partial z}y(y-d). \tag{5}$$

From the continuity equation, $\partial v_x/\partial_x + \partial v_z/\partial z = 0$, and (4) and (5) we find

$$\frac{\partial^2 p}{\partial x^2} + \frac{\partial^2 p}{\partial z^2} = 0, \tag{6}$$

which is just the Laplace equation that describes a Hele–Shaw flow.

To solve this equation, we must impose boundary conditions on the menisci bounding the fluid in the cell. Neglecting surface tension, we take

$$\sigma_{xx} - p = -p_{atm}, \quad x = \pm\tfrac{1}{2}L, \tag{7}$$

$$\sigma_{zz} - p = -p_{atm}, \quad z = \pm\tfrac{1}{2}W, \tag{8}$$

where L and W are the length and width, respectively, of the flow cell, and σ_{xx} and σ_{zz} are the viscoelastic normal stresses produced by the base shear flow. These normal stresses are taken to be uniform throughout the fluid. Without loss of generality, we can set $\sigma_{zz} = -p_{atm}$, which implies that $\sigma_{xx} = N_3 - p_{atm}$. Hence $p = N_3$ at $x = \pm\tfrac{1}{2}L$; $p = 0$ at $z = \pm\tfrac{1}{2}W$. Thus, the third normal stress difference generates a pressure difference $\Delta p = N_3$ between the sample edges at $x = \pm\tfrac{1}{2}L$ and those at $z = \pm\tfrac{1}{2}W$. Such a pressure difference can drive the Hele-Shaw-like flow illustrated in figure 14.

From (4) and (5), the magnitude of this flow near $y = \tfrac{1}{2}d$ is

$$v_x \sim \frac{1}{8\eta}d^2\frac{\partial p}{\partial x}. \tag{9}$$

The average pressure gradient is of order $N_3/(\tfrac{1}{2}L)$, so the Hele-Shaw velocity should be roughly

$$v_x \sim \frac{1}{4\eta}\frac{d^2}{L}N_3. \tag{10}$$

For a Weissenberg number around unity, $N_3/\eta \sim N_1/\eta \sim \dot{\gamma}$. Thus $v_x \sim \gamma d^2/(4L)$. For $\dot{\gamma} \approx 1\ \mathrm{s}^{-1}$, $d = 500\ \mu\mathrm{m}$, $L = 4\ \mathrm{cm}$, we obtain $v_x \sim 1.5\ \mu\mathrm{m\ s}^{-1}$, which is of the correct order of magnitude.

Equation (10) predicts that the Hele-Shaw flow should be strongly suppressed at small gaps d; the strength of the suppression is, however, dependent on the stress or shear-rate dependent boundary conditions at the glass plates, which are at present largely unknown. A thorough study of this secondary flow for various gaps would be required to develop a complete theory, and this is outside the scope of the present work. Nevertheless, the preliminary analysis given here seems to give a flow pattern in the (x, z)-plane that is qualitatively correct. Furthermore, we would expect this flow to be sensitive to the shape of the menisci at the edges of the fluid, if, as we have assumed, the impetus for secondary flow results from the boundary condition at these edges. This, as noted earlier, seems to be the case.

If, as we are convinced, this Hele-Shaw-like flow is driven by normal stresses, it is analogous to a well-known class of secondary flows that arise in viscoelastic fluids because of normal-stress-driven incompatibilities of the base flow with the equations

of momentum conservation (Larson 1992*a*). Other secondary flows driven by such incompatibilities include flow through a pipe with a non-circular cross-section, flow through a bent tube, and ordinary cone-and-plate flow with a non-negligible cone angle (Giesekus 1965). In all these flows, the simple flow field (which satisfies the momentum balance equations for Newtonian fluids) generates normal-stress contributions in viscoelastic fluids that are unbalanced; balance is restored by the secondary flow. Plane-Couette flow, however, differs from other flows in which secondary fluid flow is observed in one important respect: in plane-Couette flow no incompatibility exists in the equations of motion for the bulk fluid, it instead results because of the boundary conditions at the free edges. The secondary flow might then be suppressed by using plates of very large area, or by partially sealing of one or more edges of the sample with an immovable boundary, thereby eliminating the meniscus on one or more sides of the sample.

Plane-Couette flow has hitherto been considered free of instabilities and secondary flows, even for viscoelastic fluids. Now, however, we find that normal-stress-driven secondary flow exists even for plane-couette flow. It therefore joins the ranks of many other 'simple' geometries that display secondary flow for viscoelastic fluids, including those with normal-stress incompatibilities mentioned above, and those that produce normal-stress-driven instabilities such as torsional shear and Taylor–Couette geometries (Larson 1992*a*). It therefore appears that for viscoelastic fluids there is not a single flow geometry that is completely free of secondary flows!

5. Summary

Using suspended particles whose motions can be viewed by an optical microscope, we have shown that for entangled poly(styrene) solutions there is slip flow within 1 μm or so of solid surfaces during shear flow. The slip is driven by polymer orientation or stress, and hence continues to occur even after the solid surface driving this flow stops moving. The ratio of the slip velocity to the shear rate $V_s/\dot{\gamma}$ gives an extrapolation length of 4 and 40 μm for 8% and 20% solutions of poly(styrene) (molecular weight, 2×10^6) in tricrecyl phosphate. This magnitude of slip is similar to that observed in melts, and is consistent with the magnitude expected from the Brochard–de Gennes theory of slip. For these solutions, a transition to massive slip, or 'waveform decay', such as that seen in some polymer melts, is not observed.

In addition to slip, towards the edges of the sample a bulk secondary flow was observed with a flow pattern in the sample plane similar to Hele–Shaw flow. We argue that this flow is driven by the incompatibility between the normal stresses and the boundary condition of uniform atmospheric pressure at the free edges of the viscoelastic fluid.

REFERENCES

ARCHER, L. A., CHEN, Y.-L. & LARSON, R. G. 1995 Delayed slip after step strains in highly entangled polystyrene solutions. *J. Rheol* **39**, 519–525.

ARCHER, L. A. & LARSON, R. G. 1995 Slip flow in bulk viscous liquids. *Rheol. Acta* (submitted).

BENBOW, J. J. & LAMB, P. 1963 New aspects of melt fracture. *Soc. Petrol. Engrs Trans.* **3**, 7–17.

BLAKE, T. 1990 Slip between a liquid and a solid: D. M. Tolstoi's (1952) theory reconsidered. *Colloids Surfaces* **47**, 135–145.

BLYLER, L. L. & HART, A. C. 1970 Capillary flow instability of ethylene polymer melts. *Polymer. Engng Sci.* **10**, 193–203.

BROCHARD, F. & GENNES, P. G. DE 1992 Shear-dependent slippage at a polymer/solid interface. *Langmuir* **8**, 3033–3037.

CHEN, C. J. & EMRICH, R. J. 1963 Investigation of the shock-tube boundary layer by a tracer method. *Phys. Fluids* **6**, 1–9.

CHEN, Y.-L., LARSON, R. G. & PATEL, S. S. 1994 Shear fracture of polystyrene melts and solutions. *Rheol. Acta* **33**, 243–257.

CHURAEV, N. V., SOBOLEV, V. D. & SOMOV, A. N. 1984 Slippage of liquids over lyophobic solid surfaces. *J. Colloid Interface Sci.* **97**, 574–581.

DEMARQUETTE, N. R. & DEALY, J. M. 1992 Nonlinear viscoelasticity of concentrated polystyrene solutions: sliding plate rheometer studies. *J. Rheol* **36**, 1007–1032.

FERRY, J. D. 1980 *Viscoelastic Properties of Polymers*, 3rd edn. John Wiley & Sons.

FULLER, G. G. 1990 Optical rheometry. *Ann. Rev. Fluid Mech.* **22**, 384–400.

GALT, J. C. & MAXWELL, B. 1964 Velocity profiles for polyethylene melts. *Modern Plastics* **42**, 115–189.

GIESEKUS, V. H. 1965 Sekundarstromungen in viskoelastischen flussigkeiten bei stationarer und periodischer bewegung. *Rheol. Acta* **4**, 85–101.

HATZIKIRIAKOS, S. G. & DEALY, J. M. 1991 Wall slip of molten high density polyethylene. I. Sliding plate rheometer studies. *J. Rheol.* **35**, 497–523.

HATZIKIRIAKOS, S. G. & DEALY, J. M. 1992*a* Wall slip of molten high density polyethylene. II. Capillary rheometer studies. *J. Rheol.* **36**, 703–741.

HATZIKIRIAKOS, S. G. & DEALY, J. M. 1992*b* Role of slip and fracture in the oscillating flow of HDPE in a capillary. *J. Rheol.* **36**, 845–884.

JOHNSON, S. J., FRATTINI, P. L. & FULLER, G. G. 1985 Simultaneous dichroism and birefringence measurements of dilute colloidal suspensions in transient shear flow. *J. Colloid Interface Sci.* **104**, 440–455.

KALIKA, D. S. & DENN, M. M. 1987 Wall slip and extrudate distortion in linear low-density polyethylene. *J. Rheol.* **31**, 815–834.

KORAN, F. 1994 M. Eng. dissertation, Chemical Engineering, McGill University, Montreal

LARSON, R. G. 1992*a* Instabilities in viscoelastic flows. *Rheol Acta* **31**, 213–263.

LARSON, R. G. 1992*b* Flow-inducing mixing, demixing, and phase transitions in polymeric fluids. *Rheol Acta* **31**, 497–520.

LARSON, R. G., KHAN, S. A. & RAJU, V. R. 1988 Relaxation of stress and birefringence in polymers of high molecular weight. *J. Rehol.* **32**, 145–161.

LARSON, R. G. & MEAD, D. 1992 Development of orientation and texture during shearing of liquid crystalline polymers. *Liq. Cryst.* **12**, 751–768.

LIM, F. J. & SCHOWALTER, W. R. 1989 Wall slip of narrow molecular weight distribution polybutadienes. *J. Rheol.* **33**, 1359–1382.

MAGDA, J. J., LEE, C.-S., MULLER, S. J. & LARSON, R. G. 1993 Rheology, flow instabilities, and shear-induced diffusion in polystyrene solutions. *Macromolecules* **26**, 1696–1706.

MIGLER, K. B., HERVET, H. & LEGER, L. 1993 Slip transition of a polymer melt under shear stress. *Phys. Rev. Lett.* **70**, 287–290.

OTTER, J. L. DEN, WALES, J. L. S. & SCHIJF, J. 1967 The velocity profiles of molten polymers during laminar flow. *Rheol. Acta* **6**, 205–209.

PIAU, J. M., EL KISSI, N. & TREMBLAY, B. 1990 Influence of upstream instabilities and wall slip on melt fracture and sharkskin phenomena during silicones extrusion through orifice dies. *J. Non-Newtonian Fluid Mech.* **34**, 145–180.

PRIEVE, D. C., JHON, M. S. & KOENIG, T. L. 1985 Anomalous migration of a rigid sphere in torsional flow of a viscoelastic fluid. II Effect of shear rate. *J. Rheol.* **29**, 639–654.

RAMAMURTHY, A. V. 1986 Wall slip in viscous fluids and influence of materials of construction. *J. Rheol.* **30**, 337–357.

REITER, G., DEMIREL, A. L. & GRANICK, S. 1994 From static to kinetic friction in confined films. *Science* **263**, 1741–1744.

VAN ALSTEN, J. & GRANICK, S. 1988 Molecular tribology of ultra thin liquid films. *Phys. Rev. Lett.* **61**, 2570–2573.